Accepted Manuscript

Rapid visualization of latent fingerprints using novelCaSiO$_3$:Sm^{3+} nanophosphors fabricated via ultrasound route

R.B. Basavaraj, G.P. Darshan, B. Daruka Prasad, S.C. Sharma, Paneer Selvam, Premkumar, H. Nagabhushana

Rapid visualization of latent fingerprints using novelCaSiO$_3$:Sm^{3+} nanophosphors fabricated via ultrasound route

R.B. Basavaraj[1], G.P. Darshan[2], B. Daruka Prasad[3],S.C. Sharma[4, 5], Paneer Selvam[6], Premkumar[6], H. Nagabhushana[1,*]

[1]*Prof. C.N.R. Rao Centre for Advanced Materials, Tumkur University, Tumkur- 572 103, India*
[2]*Department of Physics, Acharya Institute of Graduate Studies, Bangalore 560 107, India*
[3]*Department of Physics, B M S Institute of Technology and Management, VTU Affiliated, Bangalore 560064, India*
[4]*Department of Mechanical Engineering, Jain University, Advisor, Jain Group of Institutions, Bangalore 560 069, India*
[5]*Avinashilingam Institute for Home Science and Higher Education for Women University, Coimbatore 641043, India*
[6]*Dept. of Radio Diagnosis, Meenakshi Medical College Hospital & Research Institute, Meenakshi Academy of Higher Education and Research, Enathur, Karrapettai Post, Kanchipuram, 631552, India*

Abstract

Latent fingerprints (LFPs) were the most significant identification card for individualization. Most commonly available fingerprints (FPs) in crime spot investigation were latent, patent and plastic. Generally, LFPs were invisible and thus the effective visualization technique necessitates for analysis of such FPs. In the past years, many traditional visualization techniques have been employed, but suffered with low resolution, sensitivity, contrast and high background noise. To overcome such limitations, we synthesized Sm^{3+} doped CaSiO$_3$nanophosphors (NPs)via an ultrasound irradiation route using mimosa pudica (*m. p.*) leaves extract as a bio-surfactant. The morphological behavior of the prepared sample was extensively studied by varying the concentration of the *m. p.* extract, ultrasound irradiation duration, pH level of the precursor solution and sonication power. The photoluminescence (PL) emission spectra exhibit characteristic peaks at ~ 561, 601 and 647 nm, which were attributed to $^5G_{5/2} \rightarrow {}^6H_J$ (*J* = 5/2, 7/2 and 9/2) transitions of Sm^{3+} ions. The Judd – Ofelt (J-O) intensity parameters and other radiative properties were estimated using PL data. The Commission International de I'Eclairage (CIE) color coordinates were positioned in orange-red region, shows average correlated color temperature (CCT) value of ~ 3576 K. The optimized sample can be used as a labeling agent for the visualization of LFPs on various porous and non-porous surfaces under normal light irradiation. The visualized FPs reveal well defined ridge characteristics, namely whorl, loop, arch, bifurcation, eye, island, bridge, sweat pores, etc. with high sensitivity, selectivity, low contrast and background hindrance. Aforementioned results evidence that the prepared novel CaSiO$_3$:Sm^{3+}NPs were promising luminescent material for solid state lighting and forensic applications.

*Corresponding author: Ph. No.: +91- 9945954010, E-mail address: bhushanvlc@gmail.com (H. Nagabhushana).

1. Introduction

FPs have been broadly investigated on the grounds that they have interesting ridge characteristics (whorl, curve and circle) and do not fluctuate with ages. The FPs have a few

minutiae's, for example, edge flow (level 1), center, delta, bifurcation (level 2) and sweat pore (level 3) which were distinctive for every person. In this manner, FPshave been utilized as the viable evidence which was critical confirmation of personal identification during crime investigations [1-4].

FPs available during crime spot investigation were classified into three types, namely patent, latent and plastic. Among, the LFPs were scarcely noticeable to naked eyes, hence it requires suitable visualization technique to make them visible. In the past decades, several visualization techniques have been followed to visualize the LFPs, namely powder dusting, ninhydrin fuming, silver nitrate spraying, iodine fuming, etc. Among these techniques, powder dusting strategy was most significant due to its rapid, lesser hazardous nature and easy to use. Generally, powder dusting technique composes of metal and magnetic powders. They were powerful in the toolfor LFPs visualization aside from a few issues. Namely, they were the low differentiation due to the non-fluorescence of the powders. Also, they have the low ridge revelation because of their resinous polymer (starch, rosin, and so forth) and colorant parts. To overcome these issues, the luminescent NPs were the best tool to visualize LFPs with well-defined ridge characteristics having high sensitivity and low background hindrance [5-10]. Hence, inorganic luminescent NPs have captured much attention in the recent years due to high surface reactivity and sensitive to the surrounding environment.

The advances in technology made the preparation techniques as simple and controlled way to obtain various NPs [11-13]. Generally, many efforts have been attempted to synthesize functional NPs, namely solution combustion route, hydrothermal, solvothermal, solid state method, sol-gel, ultrasonication route, etc. Among the existing methods, ultrasonication technique employed less power consumption, fast and eco-friendly, and was capable of producing nano/micro NPs [14].

Generally, in ultrasound assisted sonochemical method, a series of chemical reactions arise from acoustic cavitation which results in the formation, growth and sudden collapse of bubbles in the solution. As per the hotspot theory, a very high temperature (> 5000 K) was accomplished upon the collapse of a bubble. Subsequently, this collapse happens within 10^{-9} s [15]. These exciting alterations can tune the size distribution, shape and size of the powders more effectively. In order to obtain nano/micro sized materials at sensibly low temperature it was extremely indispensable for industrial applications to use ultrasound route. These conditions help to end up with NPs, which were suitable for advanced applications in optoelectronics, biotechnological and medical fields [16 -18].

Recently, silicate created numerous interests for the research community due to their characteristic features, such as stable crystal structure,high chemical resistance, high thermal and chemical stabilities, low cost, excellent water resistance, strong absorption in the near-UV region and visible light transparency. Hence, they have an attractive wide range of applications, namely, display devices, detector systems, immunoassays, scintillators, LEDs, etc.[19-23]. Among the various silicate materials, therare earth (RE) ions doped calcium silicate ($CaSiO_3$) was considered to be the best host nanomaterial due to its characteristic properties and hence they have embraced a wide range of possible applications in the fields of sensors, field emission displays (FEDs), compact fluorescent lamps (CFLs), white light emitting diodes (WLEDs), plasma display panels (PDPs), etc. [24]. Table.S1 shows the brief summary of the $CaSiO_3$ NPs obtained under different preparation methods and the experimental conditions [25-32].

In the present paper, novel Sm^{3+} doped $CaSiO_3$ NPs were prepared by ultrasound assisted sonochemical route using *m. p.* leaves extract as a bio-template. The obtained product was well characterized by powdered X-ray diffraction (PXRD), scanning electron microscopy (SEM), transmission electron microscopy (TEM), Fourier transform infrared (FTIR), diffuse reflectance spectra (DRS), X-ray photoelectron spectra (XPS) and PL studies.

Morphology of the sample was tuned by varying experimental parameters. The optimized NPs were explored as a labelling agent for visualization of LFPs on various surfaces followed by powder dusting technique.

2. Materials and Methods

2.1. Synthesis of $CaSiO_3:Sm^{3+}$ (1 mol%–11 mol%) NPs

Pure and Sm^{3+} (1 **mol%–**11 mol%) doped $CaSiO_3$ NPs were prepared via ultrasonication method using *m. p.* leaves extract as a bio-template. The precursors used were calcium nitrate hexahydrate [$Ca(NO_3)_2 \cdot 6H_2O$; Sigma Aldrich, 99.9% purity], tetraethyl orthosilicate (TEOS) [$Si(OC_2H_5)_4$; Sigma Aldrich, 99.99% purity], samarium nitrate hexahydrate [$Sm(NO_3)_3 \cdot 6H_2O$; Sigma Aldrich, 99.9% purity] and *m. p.* extract. Initially, the precursor solutions of calcium nitrate (~10.88 g) and TEOS (~10.42 ml) were dissolved in 50 mL of distilled water. The stoichiometric quantity of samarium nitrate was added to the precursor solution using a magnetic stirrer called as solution A. 5 g of *m.p.* leaves powder was dissolved in ~100 mL double distilled water (solution B) and then added slowly to the solution A. The resulting final solution (A and B) was subjected to ultrasound irradiation with frequency ~20 kHz, power ~300 W and duration period ~1–6 h at a fixed temperature of ~80 °C. At the end of the reaction, the precipitate obtained and was filtered using double distilled water and alcohol. The obtained powder was dried at ~80 °C for ~3 h in a hot air oven and further calcined at ~950 °C for ~3 h. Fig. S1. shows the schematic representation of synthesis of Sm^{3+} doped $CaSiO_3$ NPs by ultrasonication method.

2.2. Visualization of LFPs using $CaSiO_3:Sm^{3+}$ (3 mol%) NPs

A series of experiments were performed by collecting the FPs by four different donors. Before collecting the FPs, the donor hands were clearly washed with soap and gently wiped across the ridges. Then, the cleaned fingers were gently pressed on various porous and non-porous surfaces at normal pressure and room temperature (RT). The obtained FPs were latent and hence the optimized $CaSiO_3:Sm^{3+}$ (3 mol%) NPs were stained carefully on LFPs and excess powder was removed from the smooth brushing method. Finally, the developed LFPs were visualized by using 50 mm f/2.8G ED lens Nikon D3100/AF-S digital camera under normal light irradiation.

2.3. Instruments used

The structural characterization of the prepared samples was recorded using a Shimadzu made X-ray diffractometer (PXRD-7000) with Cu Kα radiation. Morphological features were studied using Table top Hitachi (SEM; Model No. 3000) and Tecnai (TEM; Model No. F-30) microscopes. A Perkin Elmer (Lambda-35) spectrometer was used to study the diffuse reflectance of the samples. The bonding position of the products was studied using Fourier transform infrared (FTIR) spectroscopy by the Perkin Elmer spectrometer (Spectrum 1000) with KBr pellets. The chemical composition was determined by X-ray photoelectron spectroscopy (XPS) using a PHI 5300 with a monochromatic Aluminum source. Photoluminescence (PL) measurements were carried out using a Flurolog-3 spectroflourimeter (Jobin Yvon, USA) with Xenon flash lamp as an excitation source. The PL decay kinetics were measured using a Hitachi made (Model no. F-4500) fluorescence spectrophotometer.

3. Results and discussion

3.1. Visualization and analysis of LFPs

Non-destructive methods for collecting evidence were significant in the field of forensic science. Due to the geometry of the substrates, non-destructive visualization of LFPs on bent surfaces remains challenging[33]. Hence, the optimized $CaSiO_3:Sm^{3+}$ (3 mol%) NPs was used for visualizing LFPs on various non-porous curved surfaces, such as soft drink can, spray bottle, goggle and TV remote followed by powder dusting method under normal light

(Fig.1). Well–defined ridge characteristics were clearly visualized with better contrast between the farrows and furrows due to its nano-regime and better adherence on the ridges.

In order to evidence the sensitivity and low background hindrance of the $CaSiO_3:Sm^{3+}$ (3 mol%) NPs for LFPs visualization, a series of experiments were performed on various porous surfaces such as aluminum foil, magazine covers with various backgrounds and debit card (Fig.2). It can be observed from the figure that, the FPs visualized on aluminum foil and credit/debit cards clearly showed all the three levels of ridge details. On the other hand, FPs visualized on magazine covers with different background shows fewer ridge details due to the background hindrance. In addition, to authenticate quality of the visualized FPs using $CaSiO_3:Sm^{3+}$ (3 mol%) NPs, conventionally used powders, namely Fe_2O_3 and TiO_2 were selected as the controls as shown in Fig.S2. As can be seen from the figures, the LFPs visualized by using commercial powders showed poor image quality and displaying only few ridge minutiae when compared to FP visualized by the $CaSiO_3:Sm^{3+}$ (3 mol%) NPs. The obtained result further demonstrated the significant selectivity of the $CaSiO_3:Sm^{3+}$ (3 mol%) NPs in advanced forensic sciences.

Further, the LFPs collected from various donors on the aluminum foil surface were visualized by using optimized NPs under normal light, as shown in Fig.3. It was observed from the figure that, all the visualized FPs shows different ridge shapes, such as loop, arch, plain whorl and central pocket whorl, which enable personal identification. Generally, LFPs constituent of many organic and inorganic residues, namely chlorides, amino acids, urea, etc. These residues concentration remains the same over a long period. Among, hydrophobic natured amino acid residues constituent of core, polar and charged amino acids, which preferentially cover the surface of the molecule and were well adhered with the solvent through hydrogen bonds. The hydrogen bonds formation takes place when two electronegative atoms (amide N, and carbonyl O) react with the same. In the present work, the donor hydrogen bonds were undergoing covalent interaction with one amide N, while acceptor hydrogen bond electrostatically reacts with the other atom O. Hence, the superior adherence property arises may be owing to the electrostatic interactions between the O and H atoms of the $CaSiO_3:Sm^{3+}$ (3 mol%) NPs and the amino acids in the LFPs, respectively.

There were three different types of fingerprint powders; regular, metallic and luminescent. Regular fingerprint powder consists of a resinous polymer and a colorant. It is unable to develop latent fingerprint (LFP) on challenging surfaces. Use of metallic compounds is harmful for user health because of metallic powder containing meshed metals with lead, gold and silver. Although the use of fluorescent nanomaterials, including quantum dots, carbon dots, $C-SiO_2$, and conjugated polyelectrolytes (CPEs), for improving the detection limit of LFPs have been attempted (Table 1), there were still concerns regarding their low detection efficiency, complicated process involved, photo bleaching, and toxicity. The visualization was restricted only level 1 and level 2 ridge characteristics due to poor fluorescent image qualities with these powders[34-38]. Hence, luminescent NPs were highly required to visualize LFPs with superior sensitivity, little background hindrance, extraordinary efficiency, lesser toxicity and stress-free detection. In the present work optimized $CaSiO_3:Sm^{3+}$ (3 mol%) NPs were used to visualize the LFPs on complex surfaces under normal light. From the above results it can be clear that the developed LFPs exhibit all the three levels (levels 1 – 3) with high contrast, high selectivity and high efficiency when compared to the reported literature in Table 1.

Hence, in order to overcome such limitations, the LFPs were visualized using the $CaSiO_3:Sm^{3+}$ (3 mol%) NPs on the surface of aluminum foil under normal light (Fig. 4(a)). It was evident from the figure that, all three levels of fingerprint ridge patterns, such as whorl (level I), ridge end, bi-furcation, specialty, bridge, crossover, island, eye (level II) and sweat pores, incipient ridges (level 3) (Fig.4 (a)) were clearly visualized due to its good adhesion

and nano-size regime.The pixel profile of a small portion of visualized FPs is depicted in Fig.4(b). The obtained result shows that the ridges (white color) and furrows (black color) pattern were clearly distinguished. It was further evident that the optimized sample adheres only on farrows, not on the furrows. Our results show that the optimized NPs can image whole FPs with high efficiency (because the whole procedure was fast and could be finished in approximately 30 s for trained investigators), and high sensitivity (because background interference can be avoided, and sweat pores can be observed owing to the small particle size). Moreover, $CaSiO_3$:Sm^{3+} (3 mol%) NPs can be stored for a long duration without losing their luminescence capability, allowing investigators to use pre-synthesized NPs.

3.2. Microstructural analysis

Fig.S3. depicts SEM micrographs of Sm^{3+} (3 mol%) doped $CaSiO_3$NPs synthesized with different ultrasound irradiation time (1 – 6 h) and 30 mL of *m. p.* extract. Initially, ultrasound irradiation time of 1 – 3 h, small buds like structures were observed (Fig.S3). Further, the ultrasound irradiation time was increased to ~ 4 – 5 h, the small buds underwent Ostwald's ripening to form sharp petals with stacked side by side. When the ultrasound irradiation time further extended to ~ 5 h, sharp petals orderly oriented to form a flower-like structure. The SEM images of $CaSiO_3$:Sm^{3+} (3 mol%) NPs synthesized with various concentrations of *m. p.* extract (5 – 30 mL) while ultrasound irradiation time was fixed to ~ 6 h, as shown in Fig.5. When the concentration of the *m. p.* extract was 5 mL, sharp tipped hexagonal type structures stacked on above the other were observed in Fig. 5(a). These hexagonal pyramidal structures were dominated, when the *m. p.* extract concentration was increased to 10–15 mL. Further, when the *m. p.* extract concentration was increased to 20 – 25 ml, hexagonal structures were disappearing and a sharp hexagonal cone-like structures were formed (Fig. 5(d, e)). When the *m. p.* extract concentration further increased to 30 ml, self-assembled flattened hexagonal cone-like structures were observed (Fig. 5(f)).

In addition, the effect of pH on the morphology of the $CaSiO_3$:Sm^{3+} (3 mol%) NPs was investigated. When the pH of the solution maintained 1 and 5, small irregular shaped self-assembled discs were observed (Fig.6). However, when the pH increases to 9, small randomly oriented spikes were observed (Fig.6). Further, the pH level of the precursor solution was fixed to 11, orderly oriented small soft hexagonal structures were obtained. Fig. 7 shows the SEM micrographs of Sm^{3+} (3 mol%) doped $CaSiO_3$ NPs synthesized with various ultrasound frequencies (20–26 kHz) and fixed ultrasound irradiation time (6 h) and *m. p.* extract (30 mL). When the ultrasound frequency was set to ~ 20 kHz, uneven and randomly oriented cone-like structures were observed. However, with the increase of sonication power to ~ 22 kHz, cones underwent growth to form sharp hexagonal shaped cones. Further, increase of ultrasonic frequency to ~ 24 kHz, hexagonal cones orderly oriented and self-assembled on above the other. The oriented, sharp cones underwent Ostwald ripening to form petal-like morphology, when the ultrasound frequency was maintained at ~ 26 kHz.

Fig.S4 shows step by step reaction mechanism for the formation of $CaSiO_3$:Sm^{3+} (3 mol%) NPs in the presence of *m. p.* extract (30 mL) with 6 h of ultrasound irradiation time. Generally, a bio-template *m. p.* leaves extract contains major bioactive compounds and is listed in Table. S2. Out of which *Mimosine*, *Mimosinamine* and *Tyrosine* includes both amine and carboxylic acid groups which could bind to the calcium of the calcium nitrate through covalent bonds to form octahedral complexes. A hypothetical and relevant route to get well defined hexagonal pyramidal structures of $CaSiO_3$:Sm^{3+} (3 mol%) was described as shown in Fig. S4. Under ultrasonication, calcium nitrate undergoes ionization to give Ca^{2+} and NO_3^-. The ionized Ca^{2+} was coordinated with organic mass of the *m. p.* extract and leads water soluble complex. *Mimosine* and *Mimosinamine* of the extract could act as tridentate ligands and coordinated to the Ca^{2+} to form temporarily formed metal complexes having octahedral

structure Fig. S4 (Step-2). Thus obtained metal complex reacts with inorganic material ions in the system such as orthosilicic acid to give $CaSiO_3:Sm^{3+}$ SS. The calcium complex formed is not permanent and it could be replaced easily with SiO_3 of orthosilicic acid under acidic conditions. Herein formation of the complex could also take place with the other ingredients of this plant extract which mainly contains OH, COOH and/or amine groups [39]. An unusual arrangement and typical nucleation / crystallization of $CaSiO_3:Sm^{3+}$ SS were the consequence due to the formation of calcium complex with organic mass of *m. p.* Two types of $CaSiO_3$ SS were revealed in the present work, one in the presence of *m. p.* extract and the other in the absence of it. In the absence of *m. p.* extract, randomly arranged $CaSiO_3$ SS with as said morphology is shown in Fig. S5. Under ultrasonication with different irradiation time (1 - 6 h) splitting of water takes place to give H and OH radicals which further reacts with silica source, tetraethyl orthosilicate (TEOS) to give orthosilicic acid with the elimination of ethanol molecules. Further, the orthosilicic acid reacts with calcium nitrate to produce primarily formed and randomly arranged $CaSiO_3$ SS (Fig. 8).

Fig. 9(a & b) shows the TEM image of the $CaSiO_3:Sm^{3+}$ (3 mol%) NPs. It was evident from the figure that, the aggregated and irregularNPs arranged in the form of chain was observed. From HRTEM results, the interplanar distance (d) was estimated and obtained to be ~ 0.29 nm (Fig. 9(c)). The SAED patterns were in good agreement with the standard (*hkl*) values of the PXRD profiles (Fig.9 (d)). The elemental composition was confirmed in EDS spectrum, as shown in (Fig. 9(e)). It was evident from the figure that the presence of Ca, Si, O and Sm elements was confirmed and thereby it confirms the purity of the sample; however, the identified carbon and copper were due to the grid used for TEM studies.

3.3. PXRD analysis

PXRD profiles of pure and $CaSiO_3:Sm^{3+}$ (1 mol%–11 mol%) NPs are shown in Fig. 10(a). All the diffraction profiles were well matched to the perovskite structure of the triclinic system (JCPDS No. 73-1110) [40]. The patterns exhibit consistency with the pure sample. As the concentration dopant Sm^{3+} ions increased, there was a slight insignificant change in the peak intensity. No additional peaks belong to impurity/oxides were observed, indicating that the incorporation of Sm^{3+} ions do not significantly alter the overall structure of the host.

The average crystallite size (*D*) of the obtained product was estimated by using Scherrer's relation and Williamson – Hall (W-H) plot method as per literature [41]. Fig. 10(b) shows the W-H plot pure and $CaSiO_3:Sm^{3+}$ (1 mol%–11 mol%) NPs. The average crystallite size of the samples was estimated and is listed in Table 1. It was found that the crystallite size obtained from W- H plots were slightly higher than that of Scherrer's method. Thiswas due to the fact that the additional strain component included in the W-H method, which was neglected in Scherrer's method.

3.4. Fourier transform infra-red spectroscopy (FTIR) studies

The FTIR spectra of pure and $CaSiO_3:Sm^{3+}$ (1 mol%–11 mol%) NPs are shown in Fig. 10(c). The spectra exhibit a broad band ranging from ~ 840 – 1240 cm^{-1}, which was due to the asymmetric stretching vibration of Si–O–Si bond and stretching vibrations of terminal Si–O bonds. The peaks at ~ 560 and 643 cm^{-1} were attributed to the characteristic stretching vibrations of Si–O–Si bridges. The sharp peak corresponding to~ 720 cm^{-1} could be ascribed to Si–O bond, which exists in the form of SiO_3^{2-}[42]. The various modes with corresponding wavenumbers are listed in Table. S3.

3.5. Diffuse reflectance (DR) spectral studies

The DR spectra of pure and Sm^{3+} (1 mol%–11 mol%) doped $CaSiO_3$NPs were recorded at RT in the range of ~ 200–800 nm, as shown in Fig. 10(d). The spectra show dominant peaks at ~ 357, 405,446, 478, 529 and 586 nm, which were due to the transitions of the 4f electrons of Sm^{3+} from the ground-state to $^6H_{5/2} \rightarrow ^4H_{7/2}$, $^6H_{5/2} \rightarrow ^4F_{7/2}$, $^6H_{5/2} \rightarrow ^4G_{9/2}$, $^6H_{5/2} \rightarrow ^4I_{11/2}$ and $^6H_{5/2} \rightarrow ^4F_{3/2}$ transitions, respectively [43]. Further, Kubelka–Munk (K-M) theory was employed to

estimate the energy gap (E_g) of the prepared NPs. The Kubelka–Munk function F (R_∞) and photon energy ($h\nu$) was estimated using the relation[44]:

$$F(R_\infty) = \frac{(1-R_\infty)^2}{2R_\infty} \text{------------------- (1)}$$

$$h\nu = \frac{1240}{\lambda} \text{--------------------------- (2)}$$

where R_∞ and λ are the reflection coefficient and absorption wavelength, respectively. The plots of $[F(R_\infty)h\nu]^{1/2}$ versus photon energy ($h\nu$) are shown in the inset of Fig. 10(d). The E_g values of the prepared samples were estimated and are listed in Table.2.

3.6 X-ray photoelectron spectroscopy (XPS) studies

Fig.11 shows the detailed XPS studies of CaSiO$_3$:Sm^{3+} (3 mol%) NPs. The main peaks at ~ 102.2, 288, 352.73, 525.6, 535.4, 1074.52 eV correspond to the binding energy of Si 2p, Ca 2p, O 1s, C 1s and Sm 3d, respectively. Surface oxygen ratio was determined from O 1s electron core level spectra by using the relation:

$$\frac{[O_{sur}]}{[O_{sur} + O_{lat}]} = \frac{area(O_{sur})}{total\ area} \text{---------------- (3)}$$

The estimated surface oxygen ratio in CaSiO$_3$:Sm^{3+} (3 mol%) was found to be around ~ 9.846. The peaks at ~ 525.6 and 535.5 eV correspond to surface active oxygen (O$_{sur}$) and lattice oxygen (O$_{lat}$), respectively. On the basis of XRD and XPS analysis, the as-prepared sample was highly crystalline in nature [45-47].

3.6. Photoluminescence (PL) studies

Fig. 12 (a) shows excitation spectrum of CaSiO$_3$:Sm^{3+} (3 mol%) NPs monitoring at 612 nm excitation wavelength. The spectrum consists of a sharp, intense peak at ~405 nm corresponding to $^6H_{5/2} \rightarrow ^4F_{5/2} + ^4M_{7/2}$ transition. PL emission spectra of CaSiO$_3$:Sm^{3+} (1 mol%–11 mol%) NPs excited under ~ 405 nm at RT in the range 450–800 nm, as shown in Fig. 12(b). The spectra exhibits harp emission bands observed at ~563, 601 and 647, which were due to $^5G_{5/2} \rightarrow ^6H_J$ (J = 5/2, 7/2 and 9/2) transitions, respectively. Among these transitions, peaks at ~ 601 and 563 nm were purely electric dipole (ED) and magnetic dipole (MD) transitions, respectively. Fig. 12(c) depicts the asymmetric ratio of the two major emission peaks 601 nm & 563 nm. In addition, it was observed that the maximum emission intensity was observed at 3 mol%. At higher concentration (> 3 mol%), the luminescence intensity decreases due to concentration quenching effect. In the present work, the concentration quenching phenomena arise may be due to the energy transfer among dopant Sm^{3+} ions. The critical distance (R_c) between nearby Sm^{3+} ions using following relation[48].

$$R_c \approx 2\left[\frac{3V}{4X_c\pi N}\right]^{1/3} \text{---------------- (4)}$$

where V; unit cell volume (10^{-1} nm), N total Sm^{3+} sites per unit cell and X_c; critical concentration. For the CaSiO$_3$:Sm^{3+} system, N = 4, V = 0.04544 (nm)^3 and X_c = 0.03. The estimated value of R_c was found to be ~0.8975 nm. Hence, it was found that the energy transfers between Sm^{3+} ions take place due to electric multipolar interaction. According to Dexter's theory, the type of electric multipolar interaction was estimated by using the following equation;

$$\frac{1}{X} = k\left[1 + \beta(X)^{Q/3}\right]^{-1} \text{----------------- (5)}$$

7

Where X stands for Sm^{3+} ion concentration, k and β; constants, $Q = 6, 8$ and 10 for dipole – dipole, dipole–quadrupole and quadrupole–quadrupole interactions. The value of Q was determined by plotting $\lg(X)$ V/s $\lg(I/X)$ (Fig. 12(d)), which gives a straight line with a slope of -1.985 and intercept of 7.066. The Q value was close to 6, which indicate that the dipole – dipole interaction mechanism was the major cause for concentration quenching. The energy level diagram of Sm^{3+} with a cross relaxation mechanism is shown in Fig.13(a).

3.7. J-O analysis

In order to investigate the site symmetry as well as luminescence dynamics of Sm^{3+} ions in $CaSiO_3$ host, the J-O intensity parameters (Ω_2, Ω_4) and different radiative properties such as radiative transition probability (A_T), radiative (τ_{rad}) lifetime, branching ratio (β_R) and asymmetric ratio (A_{21}) were calculated. In addition, J-O analysis was aninfluential tool, which efficiently defines the spectral behavior of the rare earth doped NPs. Detailed physical interpretation J-O parameters were given by Jorgensen and Reisfeld[49]. These parameters were estimated from the PL emission spectra considering magnetic dipole allowed transition ($^5G_{5/2} \rightarrow {}^6H_{7/2}$) as the reference, since it was unchanged by the neighboring crystal field environment. The relation between radiative emission rates and the integrated emission intensities were calculated by the relations given by Feng et al. [50]. By using these relations, the values of Ω_2 and $Ù_4$ were estimated and listed in a Table 3. The variation of $Ù_2$ with different Sm^{3+} concentration indicates that Ω_2 was more sensitive to the ligand environment. This means that Ω_2 value was ascribed to the covalency and structural changes in the locality of the Sm^{3+} ion exhibiting a short range effect, whereas the Ω_4 parameter was dependent on the viscosity and dielectric constant of the host influences the long range effect. In the present work, the Ω_2 value was increased with the increase of Sm^{3+} concentration up to 5 mol%, which shows stronger covalence of Sm-O bonding and lower symmetry around the Sm^{3+} ion. Smaller values of Ω_4 indicate appreciable rigidity of the host. The radiative properties, namely radiative transition probabilities (A_T), radiative lifetimes (τ_{rad}) and branching ratios (β_R) for the excited states of Sm^{3+} ion were estimated using J–O parameters, as expressed elsewhere [51]. The radiative properties of the prepared samples were estimated and are tabulated in Table 3. The obtained value of β was found to be higher than 0.50, indicating that the present phosphor is quite useful in solid state lighting applications.

Fig.13 (b) shows the CIE diagram of $CaSiO_3$:Sm^{3+} (1 mol%–11 mol%) NPs. It was evident that the CIE coordinates were located in orange-red region. To identify the technical ability of the phosphor, correlated color temperature (CCT) was estimated by using transforming equations as discussed elsewhere [52]. The quality of white light of CCT was estimated by means of McCamy empirical formula. The CCT diagram of $CaSiO_3$:Sm^{3+} (1 mol%–11 mol%) NPs are shown in Fig. 13(c). The CIE and CCT values were estimated and are summarized in the Table 3. Color purities (CP) of the obtained samples were also estimated as per the relation given elsewhere [53, 54]. The obtained values of CP are given in Table 4.

The luminescence decay curves of Sm^{3+} (3 mol%) doped $CaSiO_3$ NPs are shown in Fig. 13(d). These curves were fitted with double exponential equations. The curves specified the possible interactions between Sm^{3+} ions. The average lift times were fitted using the following equation;

$$I = A_1 \exp\left(-\frac{t}{\tau_1}\right) + A_2 \exp\left(-\frac{t}{\tau_2}\right) \quad \text{------------------(6)}$$

where I denotes luminescence intensity; A_1 and A_2 are fitting parameters, τ_1 and τ_2 are decay constants of the exponential components. The average decay time (τ^*) of the Sm^{3+} ions was calculated using the relation;

$$\tau^* = (A_1\tau_1^2 + A_2\tau_2^2)/(A_1\tau_1 + A_2\tau_2) \quad \text{--------------------(7)}$$

The average decay time of $CaSiO_3:Sm^{3+}$ (3 mol%) NPs was estimated and found to be ~1.97 ms.

4. Conclusions

Orange-red light emitting Sm^{3+} (1 mol%–11 mol%) doped $CaSiO_3$NPs were prepared by ultrasound assisted sonochemical method using *m. p.* leaves extract as abio-template. Various nano/microstructures were obtained by controlling the reaction conditions like ultrasound irradiation time, sonication power, pH and concentration of *m. p.* leaves extract. The PXRD profiles confirm the triclinic phase of â-$CaSiO_3$. The PL intensity increases up to 3 mol% and thereafter it decreases due to concentration-quenching effect. The dipole-dipole interaction mechanism is the major cause for concentration quenching. The optimized NPs was explored as a novel labeling agent for the visualization of LFPs on various porous and non-porous surfaces under normal light irradiation followed by powder dusting method. Visualized FPs reveals well defined ridge characteristics with high sensitivity, selectivity, better contrast and low background hindrance. The adopted technique and NPs display superior performance with more efficiency because LFPs visualization procedure is rapid and can be finished in approximately 30 s for trained investigators. The spectroscopic and the photometric results indicating that present NPs was explored as a novel luminescent platform for white light emission which was applicable to solid state lighting and advanced forensic applications.

References

1. Wang M, Li M, Yang MY, Zhang XM, Yu AY, Zhu Y, et al. NIR-induced highly sensitive detection of latent fingermarks by $NaYF_4$:Yb,Er upconversion nanoparticles in a dry powder state. Nano Res. 2015;8:1800.

2. Basavaraj RB, Nagabhushana H, Darshan GP, Daruka Prasad B, Rahul M, Sharma SC, et al. Red and green emitting CTAB assisted $CdSiO_3$:Tb^{3+}/Eu^{3+} nanopowders as fluorescent labeling agents used in forensic and display applications. Dyes Pigm. 2017;147:364.

3. Darshan GP, Premkumar HB, Nagabhushana H, Sharma SC, Daruka Prasad B, Prashantha SC, et al. Superstructures of doped yttrium aluminates for luminescent and advanced forensic investigations. J Alloys Compd.2016;686:577.

4. Basavaraj RB, Nagabhushana H, Darshan GP, Daruka Prasad B, Sharma SC, Venkatachalaiah KN. Ultrasound assisted rare earth doped Wollastonite nanopowders: Labeling agent for imaging eccrine latent fingerprints and cheiloscopy applications. J. Ind. Eng. Chem. 2017;51:90.

5. Sharma V, Das A, Kumar V, Ntwaeaborwa OM, Swart HC. Potential of $Sr_4Al_{14}O_{25}$:Eu^{2+}, Dy^{3+} inorganic oxide-based nanophosphor in latent fingermark detection. J Mater Sci. 2014;49:2225.

6. Chen H, Ma RL, Chen Y, Fan LJ. Fluorescence development of latent fingerprint with conjugated polymer nanoparticles in aqueous colloidal solution. ACS Appl Mater Interfaces. 2017;9:4908.

7. Park SJ, Kim JY, Yim JH, Kim NY, Lee CH, Yang SJ, Yang HK. The effective fingerprint detection application using $Gd_2Ti_2O_7$:Eu^{3+} nanophosphors. J Alloys Compd. 2018;741:246.

8. Rohini BS, Nagabhushana H, Darshan GP, Basavaraj RB, Sharma SC, Amudha P, et al. Multifunctional applications of self - assembled 3D CeO_2:Cr^{3+} hierarchical structures synthesized via ultrasound assisted sonochemical route. J. Alloys Compd.2017;724:897.

9. Park JY, Yang HK. Novel red-emitting $Y_4Zr_3O_{12}$:Eu^{3+} nanophosphor for latent fingerprint technology. Dyes Pigm. 2017;141:348.

10. Raju GSR, Park JY, Nagaraju GP, Pavitra E, Yang HK, Moon BK, et al. Evolution of $CaGd_2ZnO_5$:Eu^{3+} nanostructures for rapid visualization of latent fingerprints. J Mater Chem C, 2017;5:4246.

11. Venkataravanappa M, Basavaraj RB, Darshan GP, DarukaPrasad B, Sharma SC, Hema Prabha P, et al. Multifunctional Dy (III) doped di-calcium silicate array for boosting display and forensic applications. J Rare Earths. 2018;36:690.

12. Singh S, Srivastava VC, Lo SL, Mandal TK, Naresh G. Morphology-controlled green approach for synthesizing the hierarchical self-assembled 3D porous ZnO superstructure with excellent catalytic activity. Microporous Mesoporous Mater. 2017;239:296.

13. Deepthi NH, Darshan GP, Basavaraj RB, Daruka Prasad B, Nagabhushana H. Large-scale controlled bio-inspired fabrication of 3D CeO_2:Eu^{3+} hierarchical structures for evaluation of highly sensitive visualization of latent fingerprints. Sens. Actuators, B.2018;255:3127.

14. Venkataravanappa M, Nagabhushana H, Darshan GP, Sharma SC, Archana KV, Basavaraj RB, et al. Facile ultrasound route for the fabrication of green emitting Ba_2SiO_4:Eu^{2+} nanophosphors for display and dosimetric applications. Mater Res Bull. 2018; 97:281.

15. Suslick KS. Rev. Applications of ultrasound to materials chemistry. Mater. Sci.1999;29:295.

16. Basavaraj RB, Nagabhushana H, Daruka Prasad B, Vijayakumar GR. Zinc silicates with tunable morphology by surfactant assisted sonochemical route suitable for NUV excitable white light emitting diodes. Ultrason. Sonochem.2017;34:700.

17. Venkatachalaiah KN, Nagabhushana H, Darshan GP, Basavaraj RB, Daruka Prasad B, Sharma SC. Blue light emitting Y_2O_3:Tm^{3+} nanophosphors with tunable morphology obtained by bio-surfactant assisted sonochemical route. Spectrochim Acta, Part A. 2017;184:89.

18. Dhanalakshmi M, Nagabhushana H, Darshan GP, Basavaraj RB, Daruka Prasad B. Sonochemically assisted hollow/solid $BaTiO_3$:Dy^{3+} microspheres and their applications in effective detection of latent fingerprints and lip prints. J Sci Adv Mater Devices.2017;2:22.

19. Venkataravanappa M, Nagabhushana H, Daruka Prasad B, Darshan GP, Basavaraj RB, Vijayakumar GR. Dual color emitting Eu doped strontium orthosilicate phosphors synthesized by bio-template assisted ultrasound for solid state lightning and display applications. Ultrason. Sonochem. 2017;34:803.

20. Huang JS, Liu RH, Liu YH, Hu YS, Chen GT, Yan CP, et al. Effect of fluxes on synthesis and luminescence properties of $BaSi_2O_2N_2$:Eu^{2+} oxynitride phosphors. J Rare Earths. 2018;36:225.

21. Linganna K, Narro-García R, Manasa P, Desirena H, Rosa E De la, Jayasankar CK. Effect of BaF_2 addition on luminescence properties of Er^{3+}/Yb^{3+} co-doped phosphate glasses. J Rare Earths.2018;36:58.

22. Wan Y, Abudouwufu T, Yusufu T, He JY, Sidike A. Photoluminescence properties and energy transfer of a single-phased white-emitting NaAlSiO$_4$:Ce^{3+},Sm^{3+} phosphor. J Rare Earths.2017;35:850.

23. Man XQ, Yu LX, Sun JJ, Li SC, Zhong JL. Synthesis and photoluminescent properties of Eu^{3+}/Dy^{3+} doped SrO-Al$_2$O$_3$-SiO$_2$ glass-ceramics. J Rare Earths. 2017;35:446.

24. Sunitha DV, Nagabhushana H, Fouran Singh, Dhananjaya N, Sharma SC, Nagabhushana BM, et al. Swift heavy ion induced structural, iono and photoluminescence properties of β-CaSiO$_3$:Dy^{3+} nanophosphor.Spectrochim. Acta, Part A.2012;93:300.

25. Wan XH, Hu AM, Li M, Chang CK, Mao DL. Performances of CaSiO$_3$ ceramic sintered by Spark plasma sintering. Mater Charact.2008;59:256.

26. Wang WZ, Zhang SY, Wang LJ, Shi HL. A facile and environmentally friendly NaClnonaqueous ionic liquid route to prepare crystalline β-CaSiO$_3$ nanowires. Mater Sci Eng C.2013;33:2288.

27. Wu J, Zhu YJ, Cheng GF, Huang YH. Microwave-assisted preparation of Ca$_6$Si$_6$O$_{17}$(OH)$_2$ and β-CaSiO$_3$ nanobelts. Mater Res Bull.2010;45:509.

28. Wu CT, Ramaswamy Y, Kwik D, Zreiqat H. The effect of strontium incorporation into CaSiO$_3$ ceramics on their physical and biological properties.Biomaterials.2007;28:3171.

29. Madesh Kumar M, Nagabhushana H, Nagabhushana BM, Suriyamurthy N, Sharma SC, Shivakumara C, et al. Synthesis, characterization and spectroscopic investigation of Cr^{3+} doped wollastonite nanophosphor. Spectrochim Acta, Part A.2014;128:403.

30. Nagabhushana H, Nagabhushana BM, Madesh Kumar M, Chikkahanumantharayappa, Murthy KVR, Shivakumara C, et al. Synthesis, characterization and photoluminescence properties of CaSiO$_3$:Eu^{3+} red phosphor, Spectrochim. Acta, Part A.2011;78:64.

31. Zhou L, Yan B. Sol-gel synthesis and photoluminescence of CaSiO$_3$:Eu^{3+} nanophosphors using novel silicate sources. J. Phys. Chem. Solid.2008;69:2877.

32. Fu LL, Yang XX, Fu ZL, Wu ZJ, Jeong JH. Hydrothermal synthesis and tunable luminescence of CaSiO$_3$:RE^{3+} (RE^{3+} = Eu^{3+}, Sm^{3+}, Tb^{3+}, Dy^{3+}) nanocrystals. Mater Res Bull. 2015;65:315.

33. Wang W, Lei X, Ye ZT, Zhao N, Yang H. The luminescent properties and latent fingerprint identification application of AlN:Ce,Tb phosphors. J Alloys Compd. 2017;705:253.

34. Fernandes D, Krysmann MJ, Kelarakis A. Carbon dots based nanopowders and their application for fingerprint recovery. Chem Commun.2015;51:4902.

35. Fernandes D, Krysmann MJ, Kelarakis A. Carbogenically coated silica nanoparticles and their forensic applications. Chem. Commun. 2016;52:8294.

36. Yu YL, Yan L, Xia ZN. Non-toxic luminescent Au Nanoclusters@Montmorillonite nanocomposites powders for latent fingerprint development. RSC Adv. 2017;7:50106.

37. Malik AH, Kalita A, Iyer PK. Development of Well Preserved, Substrate-Versatile Latent Fingerprints by Aggregation Induced Enhanced Emission Active Conjugated Polyelectrolyte.ACS Appl. Mater. Interfaces.2017;9:37501.

38. Jiang BP, Yu YX, Guo XL, Ding ZY, Zhou B, Liang H, et al. White-emitting carbon dots with long alkyl-chain structure: Effective inhibition of aggregation caused quenching effect for label-free imaging of latent fingerprint. Carbon.2018;128:12.

39. Venkataravanappa M, Nagabhushana H, Darshan GP, Daruka Prasad B, Vijayakumar GR, Premkumar HB, et al. Novel EGCG assisted ultrasound synthesis of self-assembled Ca$_2$SiO$_4$: Eu^{3+} hierarchical superstructures: Photometric characteristics and LED applications. Ultrason. Sonochem. 2016;33:226.

40. Mickens MA, Assefa Z. Tunable luminescence and white light emission of novel multiphase sodium calcium silicate nanophosphors doped with Ce^{3+}, Tb^{3+}, and Mn^{2+} ions. J. Lumin. 2014;145:498.

41. Sandhyarani A, Kokila MK, Darshan GP, Basavaraj RB, Daruka Prasad B, Sharma SC, et al. Versatile core-shell $SiO_2@SrTiO_3$:Eu^{3+},Li^{+} nanopowders as fluorescent label for the visualization of latent fingerprints and anti-counterfeiting applications. Chem Eng J. 2017;327:1135.

42. Dhoble SJ, Dhoble NS, Pode RB. Preparation and characterization of Eu^{3+} activated $CaSiO_3$, $(CaA)SiO_3$ [A = Ba or Sr] phosphors. Bull. Mater. Sci. 2003;26:377.

43. Manohar T, Prashantha SC, Ramachandra Naik, Nagabhushana H, Nagaswarupa HP, Anantharaju KS, et al. A benign approach for tailoring the photometric properties and Judd-Ofelt analysis of $LaAlO_3$:Sm^{3+} nanophosphors for thermal sensor and WLED applications. Sens Actuators, B. 2017;243:1057.

44. Suresh C, Nagabhushana H, Basavaraj RB, Darshan GP, Kavyashree D, Daruka Prasad B, et al. $SiO_2@LaOF$:Eu^{3+} core-shell functional nanomaterials for sensitive visualization of latent fingerprints and WLED applications. J Colloid Interface Sci.2018;518:200.

45. Gopi D, Shinyjoy E, Karthika A, Nithiya S, Kavitha L, Rajeswari D, et al. Single walled carbon nanotubes reinforced mineralized hydroxyapatite composite coatings on titanium for improved biocompatible implant applications. RSC Adv. 2015;5:36766.

46. Kang X, Huang S, Yang P, Ma P,Yang D, Lin J. Preparation of luminescent and mesoporous Eu^{3+}/Tb^{3+} doped calcium silicate microspheres as drug carriers via a template route.Dalton Trans.2011;40:1873.

47. Ebbert C, Grundmeier G, Buitkamp N, Kröger A, Messerschmidt F, Thissen P. Toward a microscopic understanding of the calcium–silicate–hydrates/water interface. Appl. Surf. Sci.2014;290:207.

48. Wang GQ, Gong XH, Lin YF, Chen YJ, Huang JH, Luo ZD, et al. Polarized spectral properties of Sm^{3+}: $LiLuF_4$ crystal for visible laser application. Opt. Mater. 2014;37:229.

49. Jorgensen CK, Reisfeld R.Judd-Ofelt parameters and chemical bonding.J. Less Comm. Metal.1983;93:107.

50. Jing F, Zhang HJ. Hybrid materials based on lanthanide organic complexes: a review. Chem Soc Rev.2013;42:387.

51. Kodaira CA, Brito HF, Malta OL, Serra OA. Luminescence and energy transfer of the europium (III) tungstate obtained via the Pechini method. J Lumin.2003;101:11.

52. Publication CIE no 17.4 (1987) International Lighting Vocabulary, Central Bureau of the Commission Internationale de L 'Eclairage, Vienna, Austria.

53. McCamy CS, Correlated color temperature as an explicit function of chromaticity coordinates.Color Res. Appl. 1992;17:142.

54. Basavaraj RB, Nagabhushana H, Daruka Prasad B, Sharma SC, Venkatachalaiah KN. Mimosa pudica mediated praseodymium substituted calcium silicate nanostructures for white LED application. J Alloys Compd. 2017;690:730.
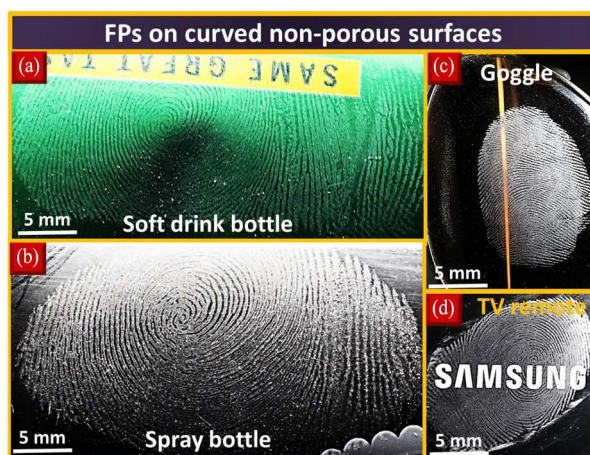
Fig.1.FPs visualized on the curved non-porous surfaces, such as soft drink can (a), spray bottle (b), goggle (c) and TV remote (d) using optimized $CaSiO_3:Sm^{3+}$ (3 mol%) NPs under normal light.
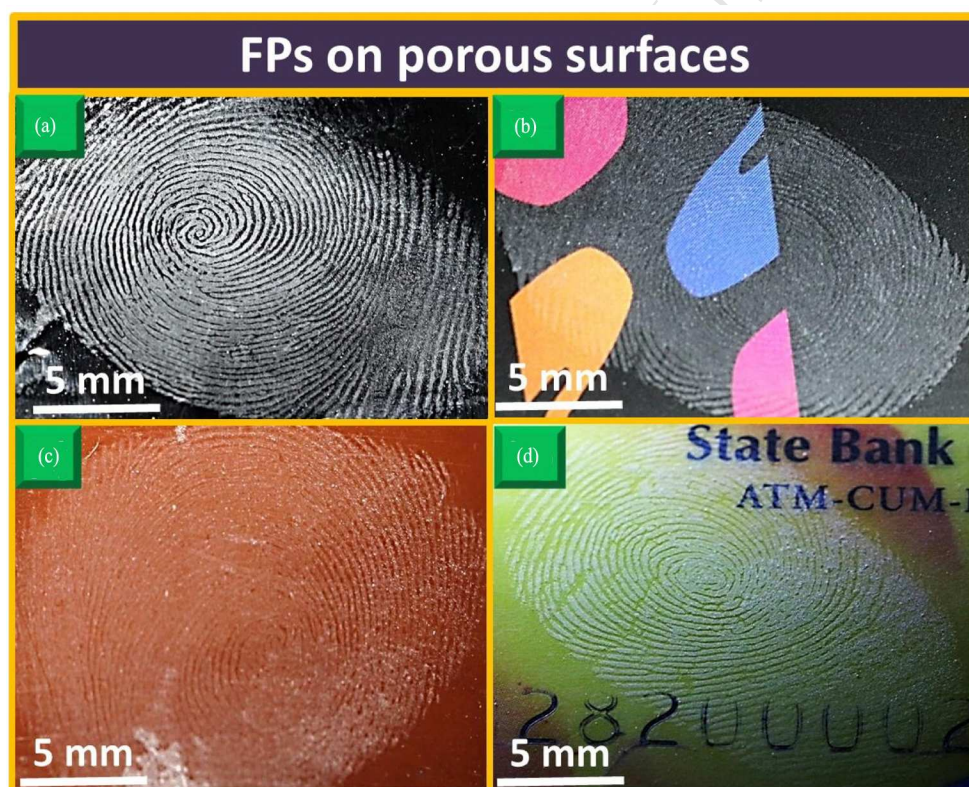

Fig.2. FPs visualized on porous surface, such as aluminum foil (a), magazine covers with various backgrounds (b, c), debit card using the optimized $CaSiO_3:Sm^{3+}$ (3 mol%) NPs under normal light (d).
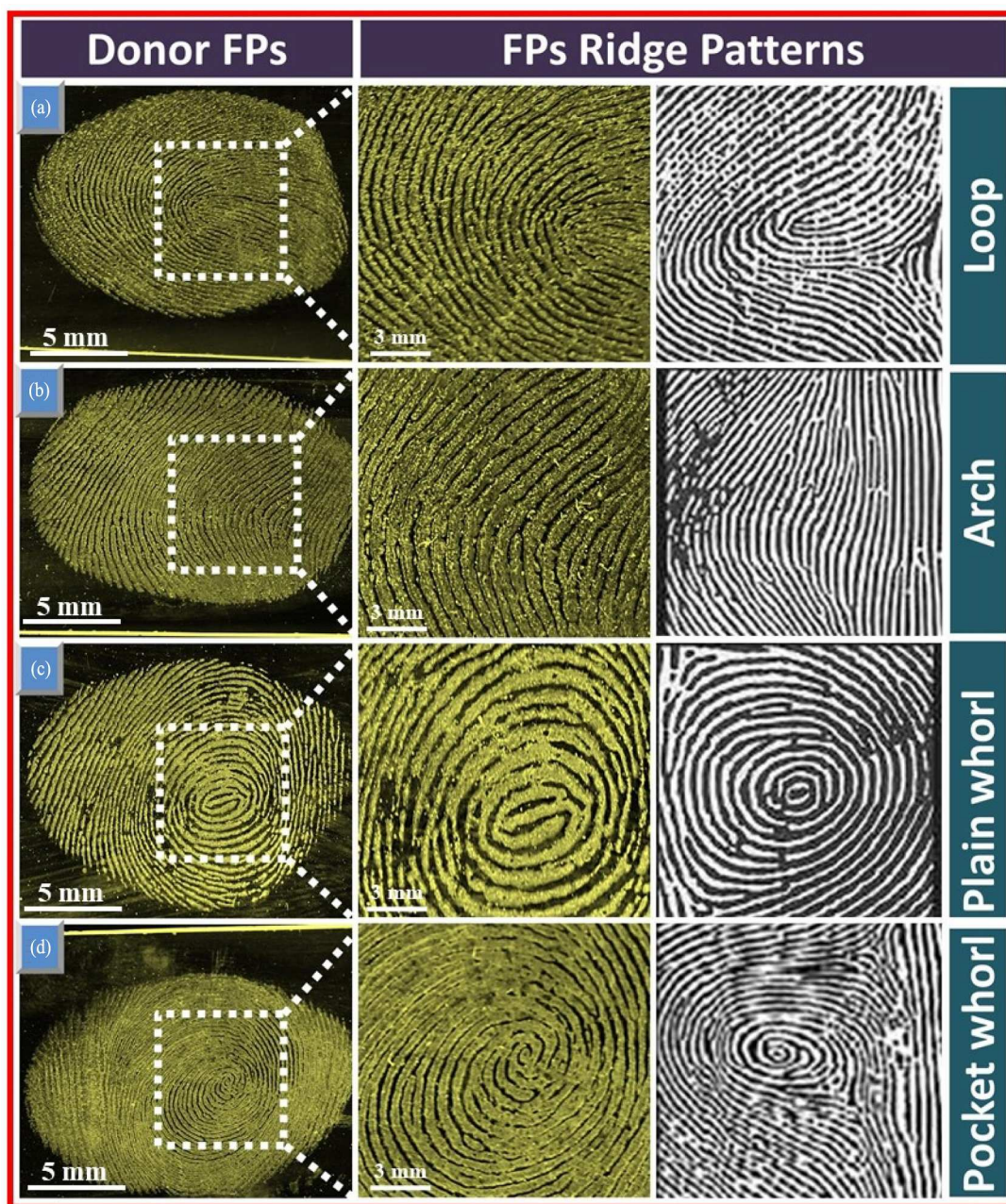
Fig.3. Various donor's FPs visualized using the optimized CaSiO$_3$:Sm^{3+} (3 mol%) NPs on aluminum foil under normal light.
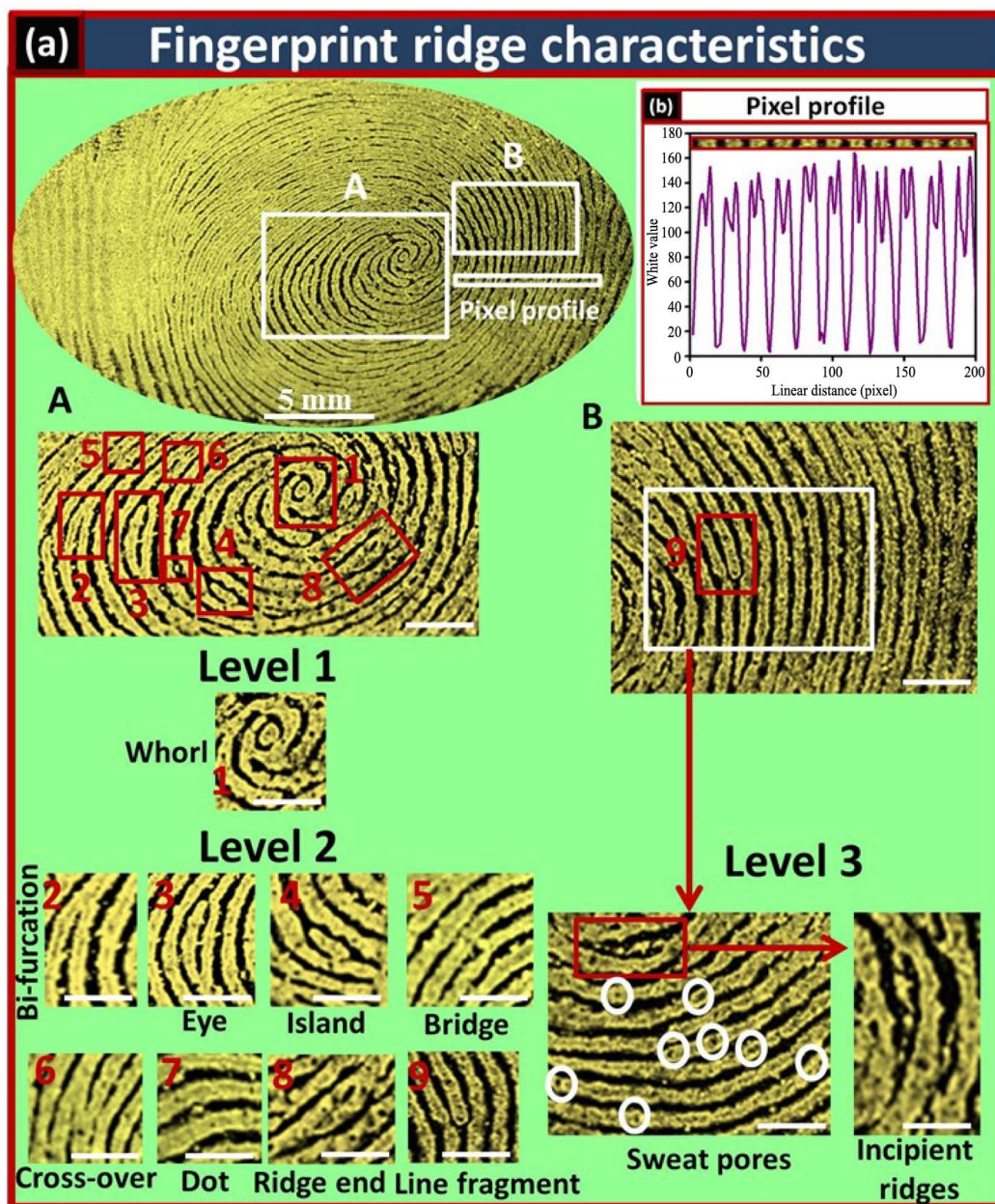
Fig.4 (a).Various ridge details revealed by using theoptimized $CaSiO_3:Sm^{3+}$ (3 mol%) NPs on aluminum foil under normal light, **(b)** Pixel profile showing the fluctuation of white value with ridge (white) and furrow (black) over a few papillary ridges indicated by rectangle box.
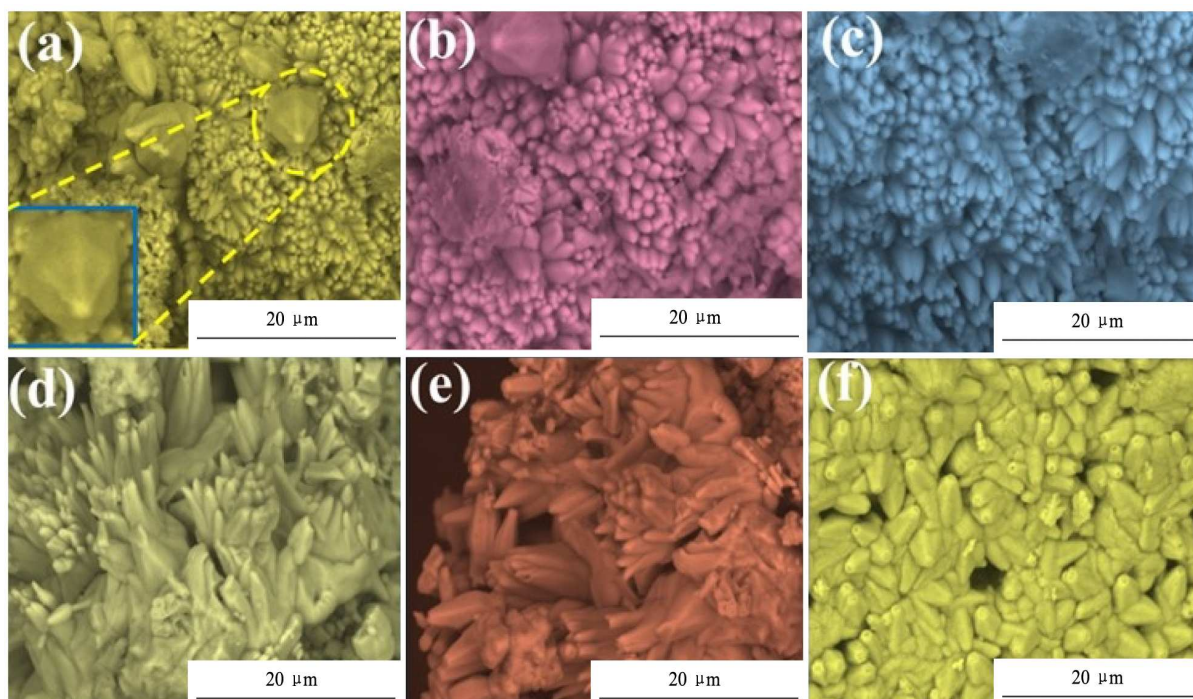
Fig.5. SEM images of CaSiO$_3$:Sm^{3+} (3 mol%) NPs prepared with different concentrations of *m. p.* leaves extract: (a) 5 mL, (b) 10 mL, (c) 15 mL, (c) 20 mL, (d) 25 mL and (f) 30 mL with 6 h of ultrasonic irradiation time.
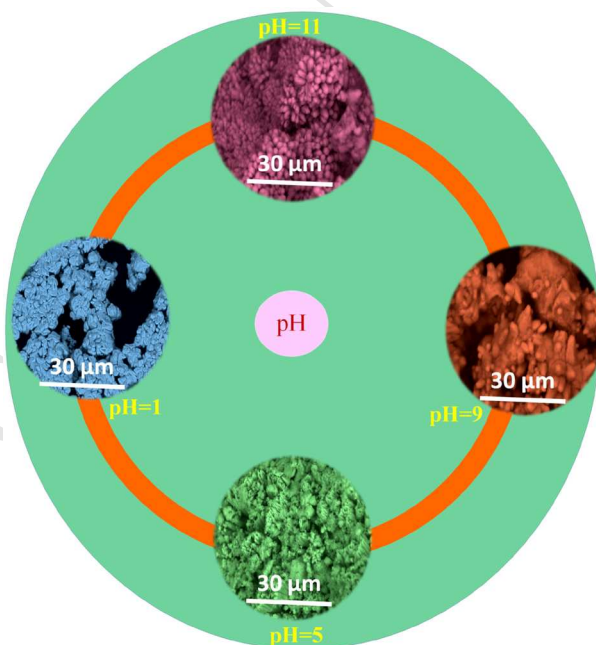
Fig.6.SEM images of CaSiO$_3$:Sm^{3+} (3 mol%) NPs prepared with various pH values (1, 5, 9 and 11) in the presence of 30 mL of *m. p.* extract.

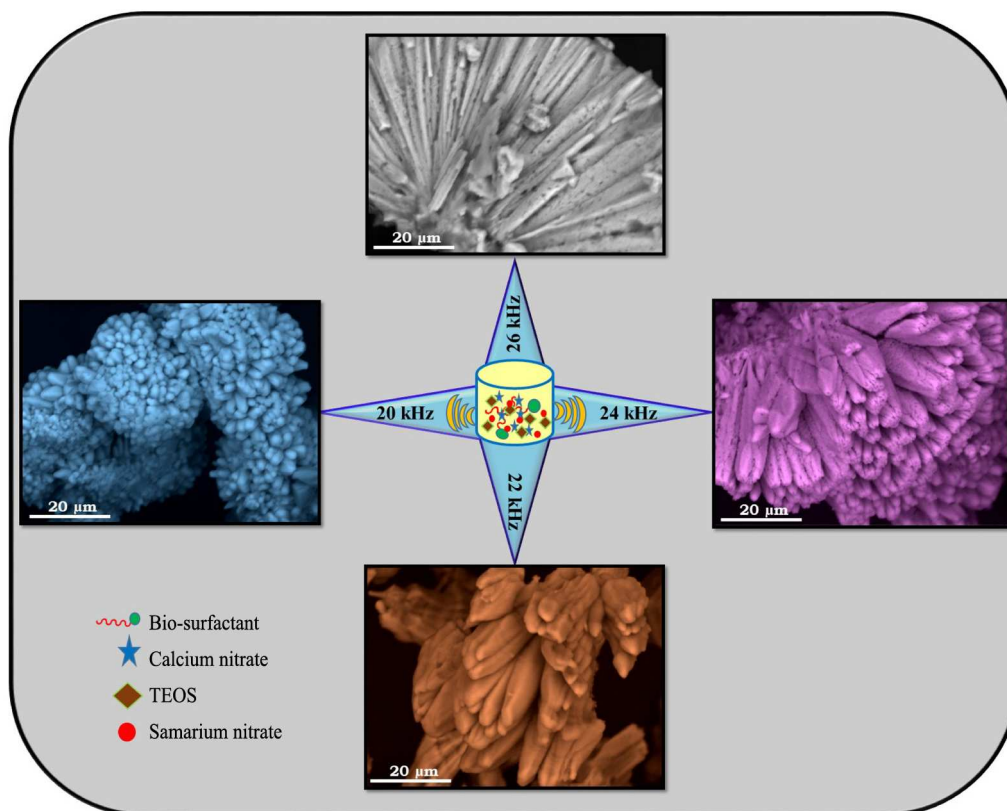Fig.7.SEM images of CaSiO$_3$:Sm^{3+} (3 mol%) SS prepared with different sonication power (20–30 kHz) and fixed ultrasound irradiation time (6 h) and *m. p.* extract (30 mL).

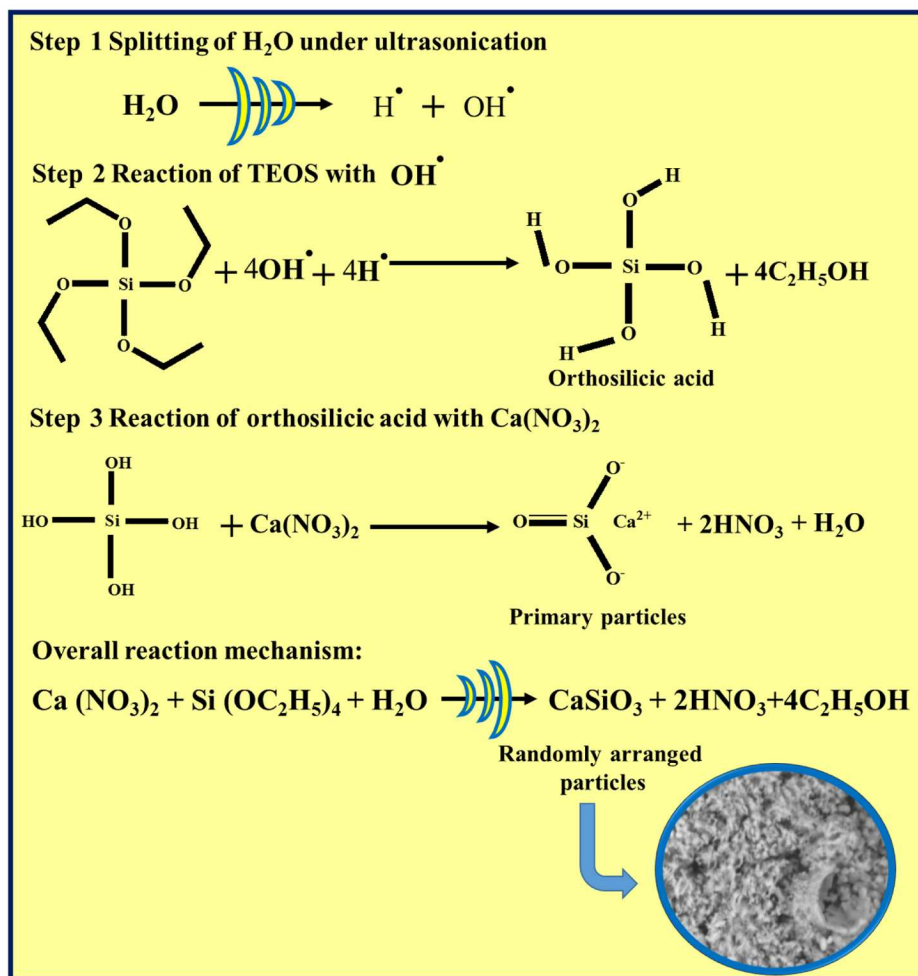Fig.8.Reaction mechanism for the formation of CaSiO$_3$:Sm^{3+} (3 mol%) NPs in the absence of
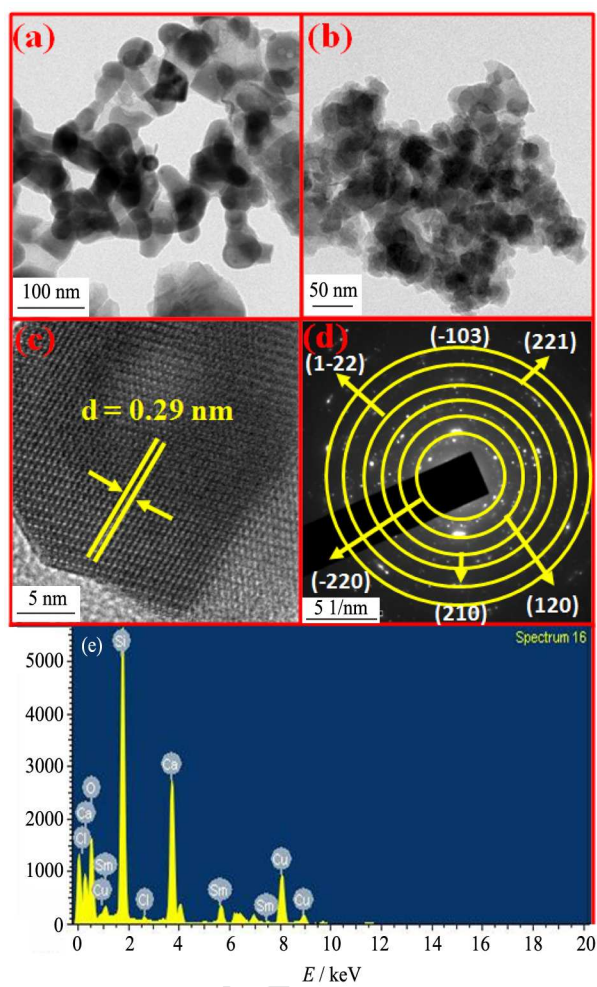*m. p.* leaves extract.

Fig.9.TEM (a, b), HRTEM image (c), SAED pattern (d) and EDS spectra (e) of $CaSiO_3$:Sm^{3+} (3 mol%) NPs.

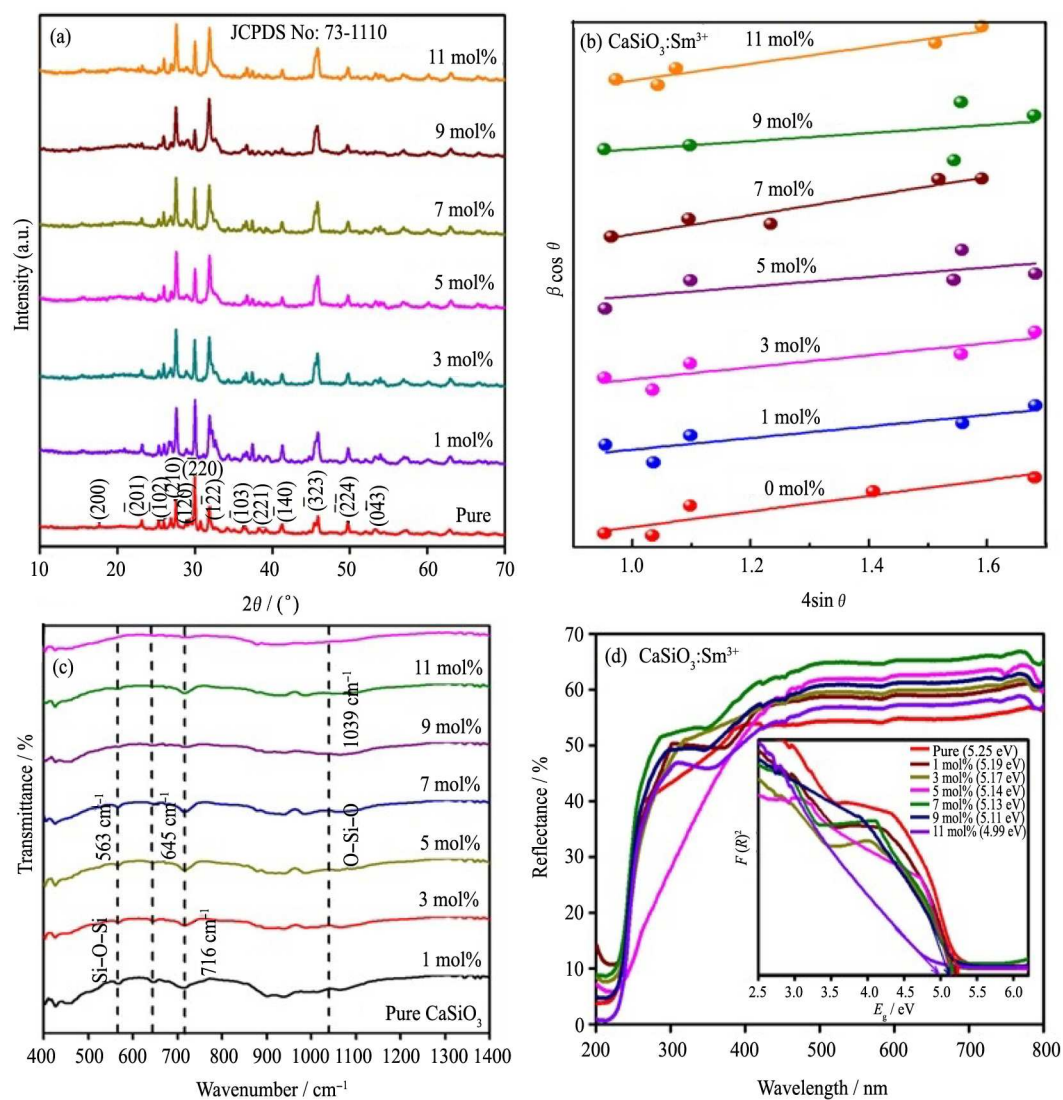Fig.10 PXRD patterns (a), W-H plots (b), FTIR spectra (c) and DR spectra (d) (Inset: energy gap spectra) of pure and doped $CaSiO_3:Sm^{3+}$ (1 mol%–11 mol%) NPs.

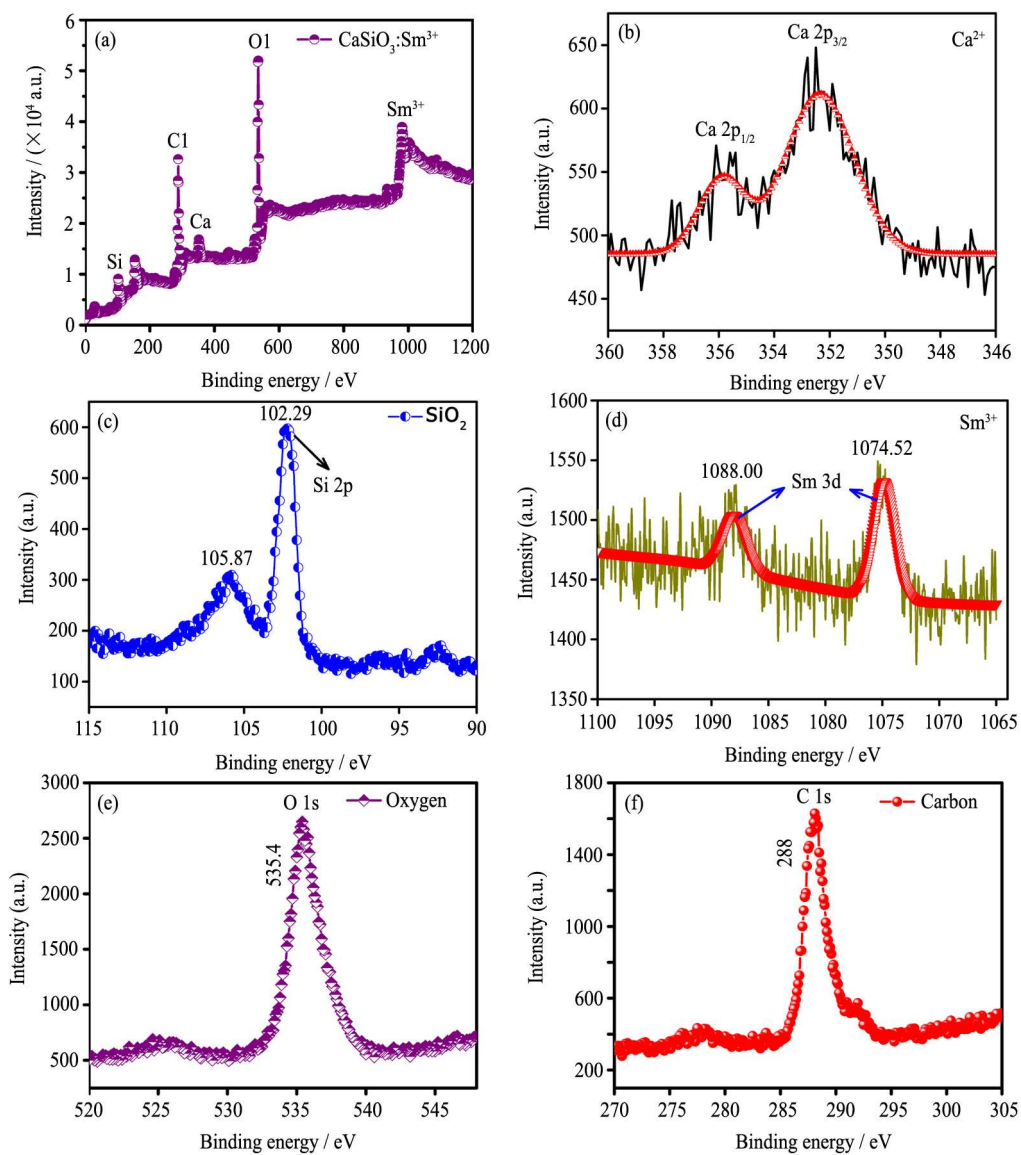Fig.11.XPS spectra of CaSiO$_3$:Sm^{3+} (3 mol%) NPs; (a) Overall scan range; (b) Ca 2$_{P3/2}$; (c) Si 2p; (d) Sm 3d; (e) O 1s; (f) C 1s peaks.
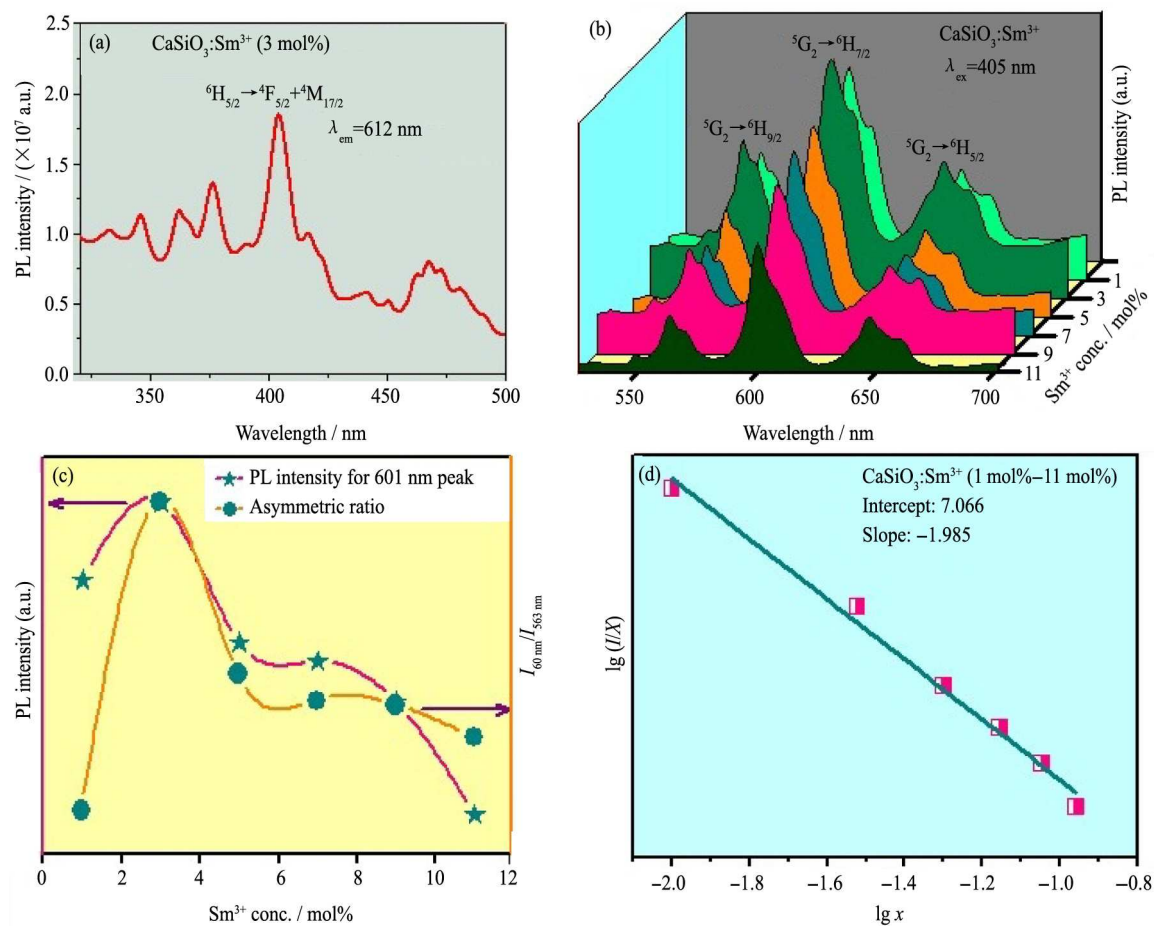
Fig.12 PL excitation spectra (a), emission spectra (b), effect of Sm^{3+} concentration on the 601 nm emission and asymmetric ratio (c) and logarithmic plot of (I/x) v/s (x) in CaSiO$_3$:Sm^{3+} (1 mol%–11 mol%) NPs (d).

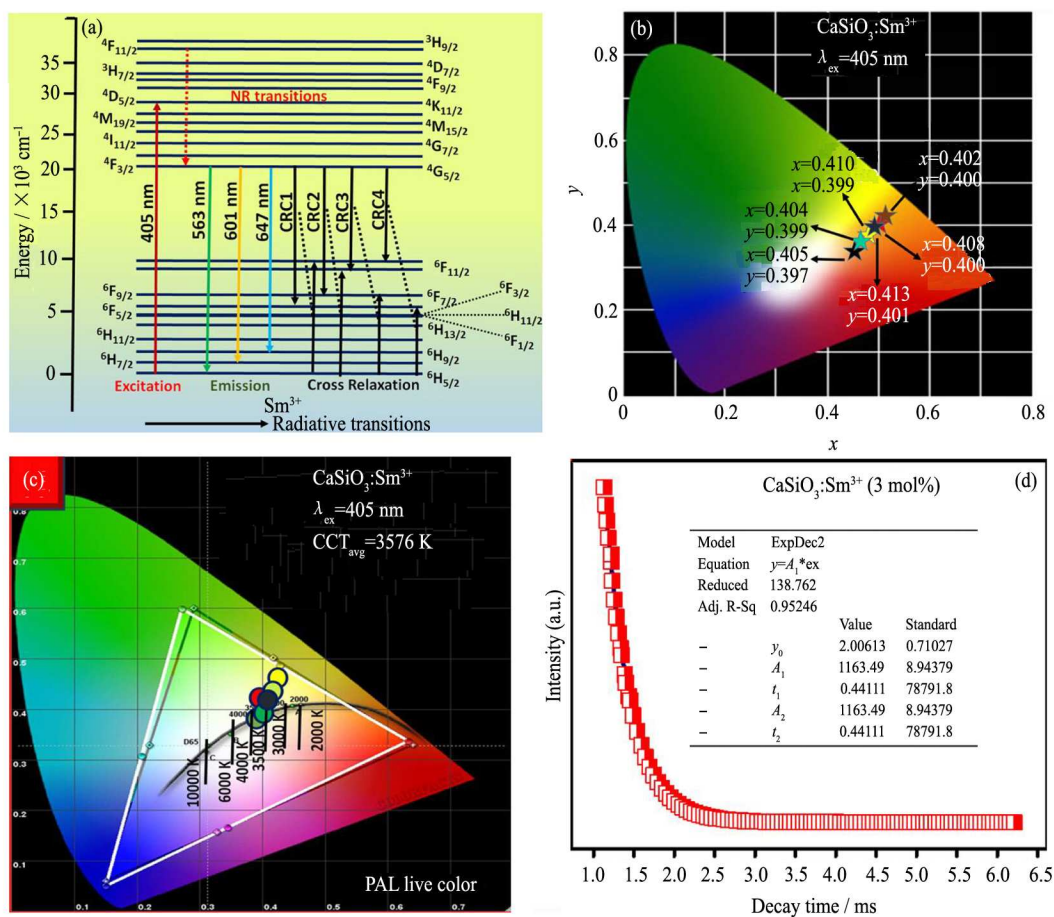Fig.13 Energy level diagram of Sm^{3+} showing a cross relaxation mechanism (a), CIE (b), CCT diagram of CaSiO$_3$:Sm^{3+} (1 mol%−11 mol%) NPs (c) and luminescence decay curve of the optimized NPs (d).

Table.1. Comparison of FP results obtained in the present study with those of reported data.

Host	FP detection method	Types of surfaces used for detection	Light source used	Level of detection	Reference
C-dots	Powder dusting	Glass slide and soft drink bottle foil	UV violet, blue and green excitation wavelength laser with a 455 nm filter	Level 1 and 2	Fernandes et al.[34]
C-SiO$_2$	Powder dusting	Cardboard and glass		Level 1 and 2	Fernandes et al.[35]
AuNCs@MMT	Powder dusting	Weighing paper, binder clips, slide glass, transparent adhesive tape, tweezers and porcelain enamel	UV irradiation (365 nm).	Level 1, 2 and 3	Yu et al.[36]
Conjugated polyelectrolytes (CPEs)	Spray method	Aluminum foil, glass slide, adhesive tape and coin	UV irradiation (365 nm)	Level 1, 2 and 3	.Malik et al. [37]
White emitting CDs (WCDs)	Immersion method	Microscopic glass slide	UV irradiation (365 nm)	Level 1 and 2	Jiang et al.[38]
CaSiO$_3$:Sm^{3+}	Powder dusting	**Non-porous curved surfaces:** Soft drink can, glass bottle, cool drink bottle, spray bottle, TV remote and goggle **Porous surfaces:** Aluminum foil, magazine covers with various backgrounds, credit and debit cards	Normal white light	Level 1, 2 and 3	**Present work**

Table.2. Estimated crystallite size, strain and E_g values of pure and Sm^{3+} (1 mol%–11 mol%) doped $CaSiO_3$ NPs.

| Sm^{3+} conc. (mol%)	Crystallite size (nm)		Strain ε ($\times 10^{-3}$)	Energy gap (E_g) in eV
	Scherrer's	W-H		
Pure	40	40	1.01	5.25
1	34	45	1.02	5.19
3	31	43	1.10	5.17
5	31	30	1.12	5.14
7	27	31	1.27	5.13
9	26	20	1.34	5.11
11	22	21	1.45	4.99

Table.3. J-O intensity parameters (Ω_2, Ω_4), radiative transition probability (A_T), calculated radiative lifetime (τ_{rad}), branching ratio (β_R) and asymmetric ratio (A_{21}) of $CaSiO_3$: Sm^{3+} (1 mol%–11 mol%) NPs.

Sm^{3+} conc. (mol%)	J–O intensity parameters ($\times 10^{-20}$ cm^2)		A_T (s^{-1})	τ_{rad} (ms)	β_R	A_{21}
	Ω_2	Ω_4				
1	2.35	1.89	332	30.07	9.983	1.08
3	2.74	2.32	284	35.16	9.985	1.05
5	2.76	2.05	282	35.42	9.988	1.04
7	2.66	1.92	292	34.16	9.974	1.05
9	2.47	1.92	315	31.73	9.994	1.06
11	2.14	1.58	312	31.25	9.998	1.05

Table.4. Photometric characteristics of $CaSiO_3$:Sm^{3+} (1 mol%–11 mol%) NPs.

Sm^{3+} conc. (mol%)	CIE		CCT		CCT (K)	CP (%)
	X	Y	U'	V'		
1	0.4027	0.4007	0.2300	0.5150	3642	94.16
3	0.4083	0.4007	0.2335	0.5158	3526	95.12
5	0.4138	0.4014	0.2368	0.5156	3418	93.18
7	0.4101	0.3996	0.2352	0.5156	3480	91.34
9	0.3947	0.3996	0.2253	0.5133	3811	90.52
11	0.3983	0.3970	0.2287	0.5128	3712	89.00

Graphical abstract
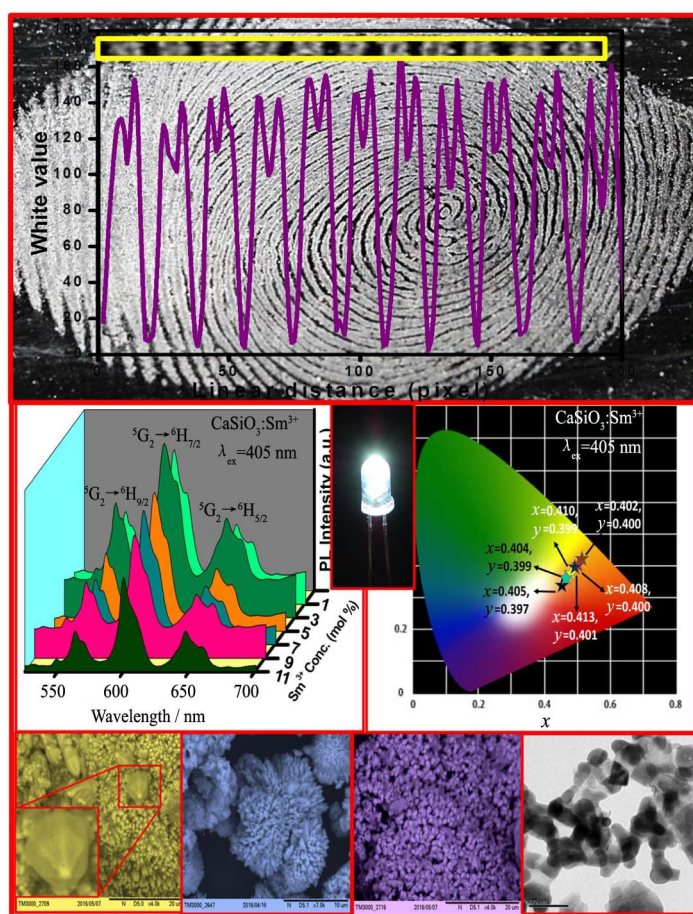
CaSiO$_3$:Sm^{3+} SS are prepared by modified ultrasound sonication method. Simple and nondestructive powder dusting method was used for visualization of LFPs. Visualized LFPs exhibits high sensitivity, reproducibility, selectivity and reliability. Morphologies are greatly dependent on pH, surfactant concentration, sonication time and power. The photometric results indicate that the optimized phosphor is highly useful in WLEDs and Forensic applications.

Research highlights

1. CaSiO$_3$: Sm^{3+} SS are prepared by modified ultrasound sonication method.

2. Simple and nondestructive powder dusting method was used for visualization of LFPs.

3. Visualized LFPs exhibits high sensitivity, reproducibility, selectivity and reliability.

4. Morphologies are greatly dependent on pH, surfactant concentration, sonication time and power.

5. The photometric results indicate that the optimized phosphor is highly useful in WLEDs and Forensic applications.